NASA CR 202124

Department of AERONAUTICS and ASTRONAUTICS
STANFORD UNIVERSITY

Final Report

for the Period

August 15, 1995 to August 14, 1996

on

APPLICATION OF PARTICLE IMAGE VELOCIMETRY TO A STUDY OF FLOW ABOUT A MULTI-ELEMENT AIRFOIL

Grant No. NCC2-5155

Submitted to

NASA-Ames Research Center
Moffett Field, California 94035-1000
James C. Ross - Technical Officer

by the

Department of Aeronautics and Astronautics
Stanford University, Stanford, California 94305

Stephen M. Walker - Research Assistant
Donald Baganoff - Principal Investigator

November 14, 1996

1. ABSTRACT

An experiment was performed on the flap tip vortex shed from a half span Fowler flap. This flap was mounted on a 5 foot span NACA 63_2-215 Mod B airfoil in the 7 by 10 foot wind tunnel at NASA Ames Research Center. Several noise reduction studies were performed with this model, and the addition of the Particle Image Velocimetry (PIV) research discussed here served as a proof case of large scale PIV. The measurement plane investigated here was a cross plane region. This is cross plane relative to the freestream flow direction. The measurement plane was located at a position 18 inches downstream of the flap trailing edge. This served to prove that measurements could also be made in the more difficult cross plane direction rather than in the downstream flow direction. Lastly the PIV data was used as a practical research tool that yielded important results that could not otherwise be obtained.

The flow field area measured was 40 cm by 40 cm square, and served to characterize the downstream flow characteristics of the flap tip vortex under three configurations. The baseline configuration which was the flap and the wing only. The baseline with the addition of a 3/4 span slat, and the baseline with a Flap Edge Device which was designed to reduce the noise generated at the flap. All configurations were tested at a freestream velocity of 64.84 m/s.

The test resulted in average velocity fields for the three configurations tested. The velocity fields aided in verifying other testing methods on this particular experiment, and also yielded further insight into the characteristics of the flap tip vortex under the three configurations considered. The velocity data was reduced, and we were able to calculate the vorticity of the flow field. From the position of minimum vorticity the location of the center of the vortex was determined. The circulation was also calculated and aided in comparing the effects of the three configurations on the lifting characteristics of the flap.

2. INTRODUCTION

Consortium Grant Number NCC2-5155 began on August 15, 1995 as a collaboration between Stanford University and NASA Ames Research Center with the expressed purpose of setting up instrumentation for large scale Particle Image Velocimetry (PIV) in the 7 by 10 foot wind tunnel located at Ames. This consortium grant covered the one year period from August 15, 1995 to August 14, 1996 and as stipulated in the agreement a final report was required at the end of the year. This document represents the final report and summary of work completed under that agreement.

The bulk of the work completed during the one year period was devoted to setting up the instrumentation for large scale PIV measurements in the 7 by 10 foot wind tunnel, located at NASA Ames Research Center, and more properly identified as 7 by 10 # 1. Although much of the preliminary and preparatory work was performed elsewhere, the bulk of the activities required to reach the desired goals were carried out in the wind tunnel. The PIV instrumentation developed for the 7 by 10 facility was intended to achieve three objectives: 1) to show that the capabilities of the PIV method can now be applied to large scale environments; 2) to show that the measurements can be made in the cross-flow plane of a complex flow field; and 3) as a practical test case to obtain data on the instantaneous velocity field near a flap edge on an existing multi-element airfoil. The multi-element airfoil testing took place during a one week period in June 1996.

The work was carried out by Stephen Walker, a graduate student at Stanford University (advisor: Professor Donald Baganoff), and by Professor Krothapalli of Florida State University. A large measure of assistance was received from Professor Louis Lourenco, also of Florida State University, and from Mehmet B. Alkislar a graduate student at Florida State University. Professor Krothapalli provided the primary liaison with NASA Ames Research Center for this work.

During the development phase of PIV, a process in which Professor Krothapalli played a major role, PIV was primarily used as a laboratory research tool, considered best suited for small scale, controlled environment experiments. In recent years PIV has been shown to be applicable to high speed flows as well. Professor Krothapalli, under a general investigation NASA contract, proposed applying PIV to large scale wind tunnel environments, and through conversations with Doctors C. A. Smith, L. E. Olsen, and J. C. Ross, all of NASA Ames Research Center, Professor Krothapalli was able to define the

goals of the study. This work represents the first step in moving the PIV method from the laboratory to wind tunnel application.

The PIV Method

The concept of Particle Image Velocimetry is a well known and straight forward technique for measuring velocity fields. The concepts that comprise the PIV method are simple and outlined here.

Particle Image Velocimetry is used to measure fluid velocities within a flow field of interest. To accomplish this end the PIV method relies on a first order approximation of velocity, so that the velocity determined is a calculated quantity. Recall that velocity can be expressed as a distance divided by time.

$$\text{Velocity} = V = \frac{\Delta x}{\Delta t}$$

This relationship can be used to calculate the velocity at a point if the distance traveled by a fluid particle originating at that point over a given time interval is known or can be determined.

Typically the flow fields of interest occur in water or in air, and determining the positions of air and water molecules is not feasible. However if the flow field is seeded with particles larger than the molecules of air or water, the positions of these larger particles can be determined. (How the positions of the larger particles are determined will be addressed shortly.) Typical tracer particle sizes range from 0.2 μm to approximately 5 μm. These larger tracer particles are then used to calculate the velocity field. It is therefore important that the larger particles follow the flow field, otherwise the velocity field calculated will not represent the true flow field. To calculate the velocity it is necessary to determine two consecutive positions of these larger particles over a short time interval. The two positions will yield the Δx distance and direction of motion, and the time interval, Δt, is known, and through these two quantities the velocity can be calculated. This is the concept upon which PIV is based.

Essentially the specifics of the PIV method are the means by which the positions of the seeding particles, which trace out the flow field of interest, are determined. The specifics of the method include: 1) the optical images, which contain the positions of the

tracer particles, and how these images are collected and saved; 2) the calculations used in determining the Δx distance traveled by the tracer particles; and 3) other technical concerns inherent to the PIV method, and the solutions to these concerns.

In order to determine the position of the seeding particles, the tracer particles, it is necessary that an optical image be captured. The image captured serves as a record of the position of the tracer particles at an instant in time. Ideally two images must be captured, although in many instances the same results can be obtained from a single double exposed image. Typically a single double exposed image is the method used for high speed flows. For simplicity the case of two distinct images will be addressed first, and then the 'single image' case will be discussed later. The two images captured are typically separated temporally by only a few microseconds (when the fluid velocity is of the order of 100 m/s and the spatial separation is 1 mm), and serve as the raw data for the PIV method. Ideally within each of the two images the positions of individual tracer particles can be determined, however within a flow field which has uniform seeding it is very difficult to identify a specific particle from one frame to the next, and this fact often changes the method used in reducing the optical image to a velocity field. Data reduction then involves determining the position to which a group of tracer particles has moved, not the position to which an individual particle has moved. Although the method of data reduction is different, the overall concept of PIV is the same whether one is concerned with a group of tracer particles or with an individual tracer particle. The exact position of a tracer particle at two separate instances of time yields what is known as a 'particle pair'. A 'particle pair' would then yield all the information necessary to calculate the velocity at a single point. Recall that the velocity is essentially calculated by computing the spatial shift of a tracer particle in each of the two images, over a known time interval. The PIV method assumes the tracer particles are small enough to faithfully follow the fluid flow, and relies upon the tracer particles being large enough to be imaged by the optical techniques used.

To illuminate the tracer particles for capturing the optical image an intense light source is required to insure that sufficient light is scattered from the particles. Lasers are used as this light source. The high intensity light that can now be achieved from modern lasers permits the use of tracer particles small enough that the tracer particles will more faithfully follow a fluid flow. The laser also provides a precise duration of illumination of the tracer particles, which will affect image quality, and a precise time interval between pulses. Keep in mind that the time interval between pulses is used in the calculation of velocity. The laser light source delivers two pulses of high intensity light temporally separated by a few microseconds, as mentioned above. The two laser pulses provide the

light source for each of the two images necessary for determining the two sequential positions of the tracer particles.

Capturing the optical images is perhaps the most crucial step in the PIV method. The raw data is contained within the images captured, and without taking lengths to insure the validity of this data the rest of the method is irrelevant. The image of the tracer particles can be captured and saved by one of two methods. The first is to capture the image on photographic film. This method results in high spatial resolution, but limits raw data processing speeds, and as a result slows down PIV data output and subsequent evaluation. The second method is to capture the image digitally using a charge coupled device (CCD camera). The CCD camera, while inferior to photographic film in spatial resolution, has many features that make it the primary technique of choice. Use of a CCD camera greatly reduces the processing time associated with capturing an image and calculating the velocity field. Processing time for each image becomes a major factor in situations where testing time is limited, and short image turnaround times permits immediate verification that usable data has been obtained. Storage and handling of images is also greatly simplified by the use of digital techniques for optical image capture. Perhaps the most significant benefit gained in moving from photographic film to the digital CCD camera occurs in terms of data reduction. The CCD camera allows hundreds of images to be captured, stored, and processed, virtually automatically, and statistical investigations can then be performed with these images. The calculations used to determine the velocity fields are generally performed by a computer. Using a computer for data reduction necessarily implies that the raw data, the optical image, be stored numerically and made accessible to the computer program employed for data reduction. In the case of photographic film, it would be necessary for the developed photograph to first be scanned before data reduction could be performed by the computer. (Several methods do exist for the evaluation of photographic film images which do not require that the photographic images be transformed into electronic images, but these will not be addressed here.)

The method used to reduce the raw data to velocity data relies on statistical correlations as the mathematical model used to accomplish this task. This is done since it is difficult to determine particle pairs, without prior knowledge of a velocity field, and finding particle pairs is nearly impossible for cases in which there are numerous particle pairs in a region. The statistical correlation is performed by first defining a small area of the first optical image. This small area is then compared to the second optical image. The resulting cross-correlation function yields a probability distribution which indicates the likelihood that the area of interest has moved to the particular position in the second image. The

location with the maximum probability from the cross-correlation function determines the calculated displacement for the area of interest. The probability distribution calculated from the correlation defines the displacement, and the time between laser pulses determines the time interval for the motion. This is how the raw data is reduced to a velocity field.

Higher speed flows make it increasingly difficult to image particle pairs without reducing the time between the two images captured, which in turn reduces the time between laser light pulses. In practice the time intervals used to capture images of tracer dictate that only a single image can be captured. This is due to limitations of the camera. There is simply not sufficient time available to permit the camera to open and close the shutter, and download the image or advance the film within the few microseconds available between laser pulses. The single optical image captured is therefore double exposed, and this single image then contains all the displacement data. In this case an auto-correlation method must be used. The mathematics of the auto correlation are the same as that of cross-correlation technique, but now only a single image is used to construct the probability distribution used to determine the displacement of an area of interest. The primary disadvantage of the single image is that directional ambiguity arises. This directional ambiguity is due to the inability to determine which sub-region was captured first in the optical image. This problem can be reduced to the case of a single particle pair for illustration. Simply stated, given an imaged particle pair, it is impossible to know which of the two particles was in fact recorded first, and for this reason it is possible that the calculated velocity field could be headed in one direction or in the opposite direction. If two optical images are captured the directional ambiguity can be avoided since it is known which image was captured first. Another advantage in using the cross correlation method, or two separate images, is that the correlation function determined has a higher signal to noise ratio which helps to improve the overall accuracy of the results.

In the wind tunnel experiment discussion that follows an additional step in complexity was taken. This additional step was performed in order to compensate for having a single doubly exposed image instead of two images. Recall that for a single captured image the method suffers from directional ambiguity. As a means of overcoming this difficulty an artificial shift is added to the data from the second image. The artificial shift creates an additional displacement between all particle pairs in the single image. This technique is very useful and the benefits greatly outweigh any additional difficulties encountered in instituting the method. In particular the greatest benefit achieved from this spatial shift is that the directional ambiguity is removed from the problem. The artificial shift works by introducing a displacement that is significantly larger than any achievable

negative displacement in the flow field. (Here negative refers to displacements in the opposite direction to the artificial shift added to the second image.) As a result when calculating the flow field it is known that the second half of any particle pair must lie to one side. After the displacements are calculated, the displacement due to the artificial shift can be removed, and then the calculation of the velocity field is completed. It is of course necessary to calibrate the displacement due to the artificial shift.

In order to introduce the artificial spatial shift of the second image a rotating mirror assembly was used. Simply stated, this method shifts the second image to a different horizontal position in the imaging plane by changing the optical path to the recording plane. See figure 1.

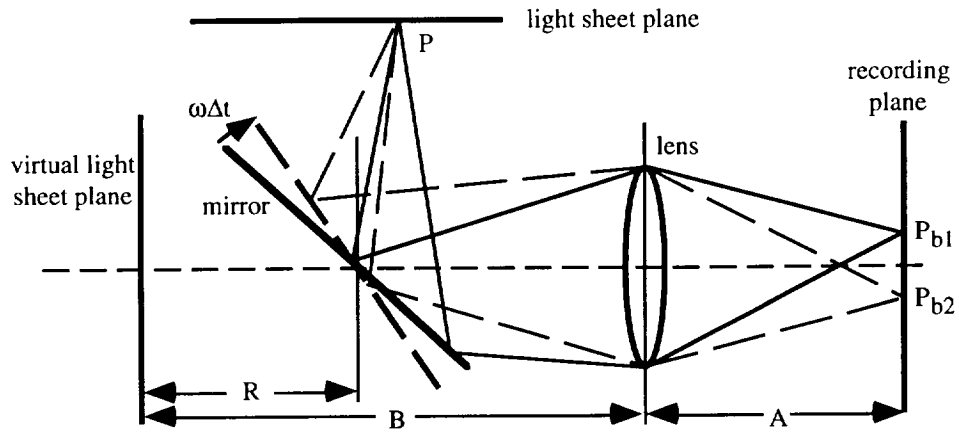

Figure 1. Illustration of the displacement of an imaged point in the recording plane due to a rotating mirror.

The mirror as it rotates will take the object point at P, and will due to its own rotation and also due to the focusing property of the lens move the image point. Figure 1 illustrates the movement of the image point at separate instances in time. The shift produced by the rotating mirror can be expressed explicitly by a simple relation.

$$X_{shift} = 2\,\omega\,R\,M\,\Delta t$$

In the above expression X_{shift} represents the shift in the position of the second image, and has the physical dimension of length. ω is the angular rotation rate of the mirror. R is the distance between the rotation axis of the mirror and the measurement plane. Note in figure 1 that the virtual light sheet plane is included to aid in showing this distance, R. M is the magnification of the lens, and Δt is the time interval between the two laser pulses. These quantities can be used to predict the horizontal shift of the second image, but in practice this quantity is calculated by using a fixed objective and effectively calibrating the value of the shift, X_{shift}.

The PIV method is conceptually simple, but technically difficult in application. Timing of each of the components, (laser, camera, rotating mirror), becomes essential for the success of the PIV method. It is therefore necessary that each component operate in the appropriate temporal order to accomplish the overall goal of the system. Fortunately as the PIV method has evolved so has the technology, and specifically the hardware. Each of the components, the camera, the laser, the rotating mirror, and the associated hardware is routed through a computer, and the relative timing is maintained by the computer's own operations. The PIV software has primary control of all of the components, and it greatly simplifies the raw data collection.

To further stress the importance of this experiment, note that Particle Image Velocimetry, although well established and evolved, has primarily been used for small scale studies. In the wind tunnel experiment described herein the relative scale has been increased by an order of magnitude. The wind tunnel is 7 feet high by 10 feet wide. The chord of the wing model is 2.5 feet and the span is 5 feet. The vortical structure created by the half span flap in this experiment is considered to be approximately 1.5 feet square. A measurement field of this size is not well suited for point wise measurements, and although the complexity of the PIV method does increase with the larger scales considered here, the evolution of PIV has reached a level where PIV is appropriate for this type of study. In particular the PIV method yields an entire velocity field for the area of study; this avoids the time necessary for point wise measurement methods. Also the flow field of study here is hostile and highly turbulent. The hostile environment makes it difficult to position and hold steady any type of probe which would be necessary for an intrusive method. Lastly intrusive methods may have adverse effects on the flow field characteristics, which would have to be determined by further studies. The non-intrusive optical technique of the PIV method is well suited for the testing environment considered in this experiment, and yields additional data that would otherwise be difficult to obtain.

3. EXPERIMENT

The experiment was carried out in the 7 by 10 wind tunnel at NASA Ames Research Center. The wind tunnel, (7 x 10 #1), is a closed circuit wind tunnel with an optimal test section area 7 feet high and 10 feet wide, and with the test section having a length of 15 feet. The wind tunnel is driven by a DC motor with a maximum power output of 1600 hp, which yields a maximum free stream velocity, empty test section, of 116 m/s. Figure 2 is a schematic drawing of the wind tunnel and the experimental setup used in the test.

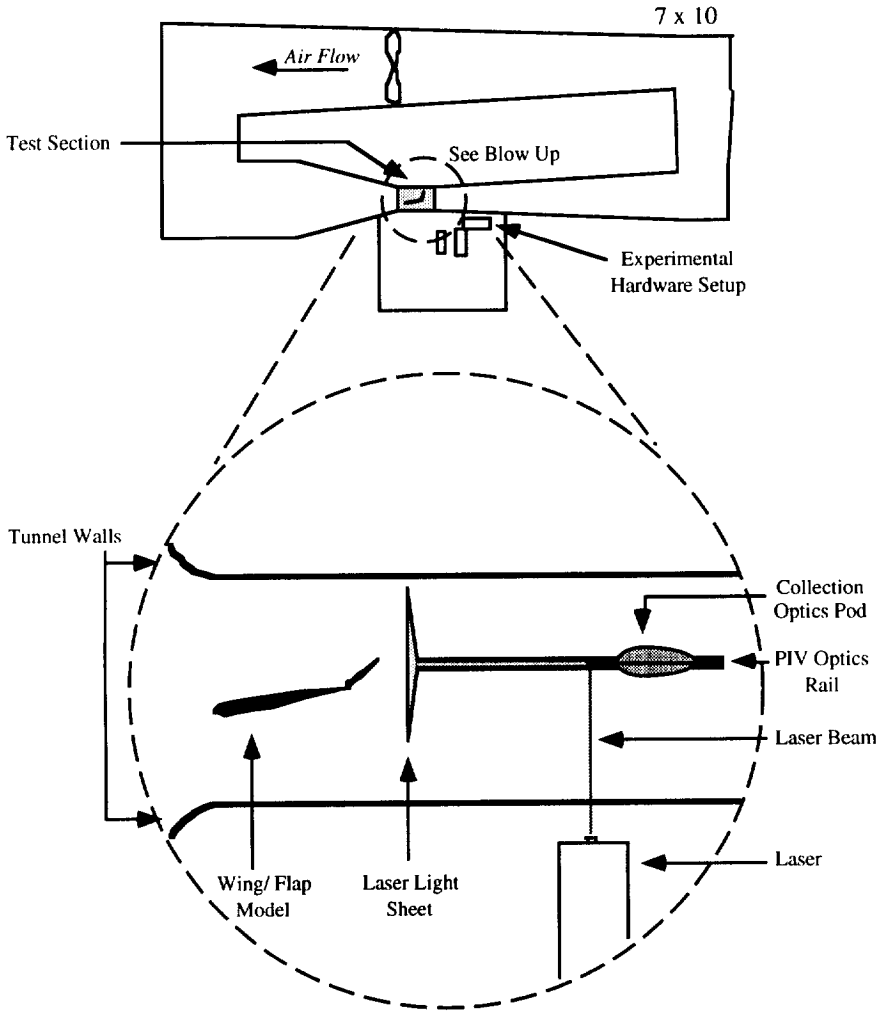

Figure 2. Illustration of 7 x 10 wind tunnel and experimental setup.

The wing model tested was a 5 foot span NACA 63_2-215 Mod B profile airfoil. The chord, c, of the wing was 2.5 feet, and the wing was fixed at an angle of attack of 10° throughout the test. This wing profile was coupled with a half span Fowler flap, which had a 9 inch chord, (0.30 c). The flap was fixed at an angle of attack of 39°. The finite wing and the Fowler flap formed the baseline model configuration for this experiment. The wing model was mounted vertically in the 7 by 10 wind tunnel. The wing was mounted between two ground planes that served to remove the boundary layer of the wind tunnel from aerodynamic interaction with the model. Figure 3 is a photograph of the model installed within the wind tunnel. The photograph shows the baseline configuration, the wing and the flap, with the addition of a 3/4 span leading edge slat.

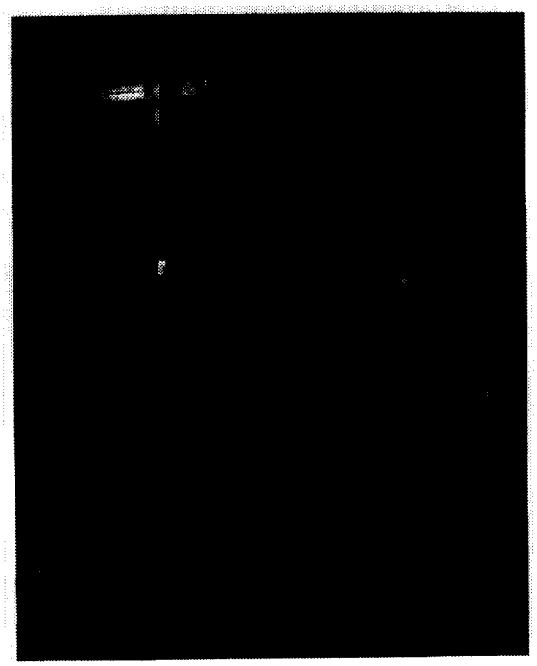

Figure 3. Photograph of model in wind tunnel. (Configuration shown is baseline with the 3/4 span slat.)

This baseline configuration was also tested with the 3/4 span leading edge slat. The profile shape of this high lift device was designated as an LB-546 slat. The slat had a chord of 4.5 inches, or 0.15 c, where c was the wing chord. The slat was at an angle of attack of 10°.

The other addition to the baseline configuration tested was a flap edge device. The flap edge device is referred to as the Full Size Flap Tip Fence. The flap edge device mounts to the side plane of the Fowler flap, and when properly mounted the upper edge of the Full Size Flap Tip Fence is flush with the upper surface of the flap. In this position the flap edge device extends one full flap thickness beyond the lower surface of the flap. This is the reason it is called the Full Size Flap Tip Fence. There were other Flap Tip Fences with varying overlap beyond the lower surface of the flap, each fence was designated by the amount of overlap. This particular fence was used in these tests due to its high noise suppression. Figure 4 illustrates the shape of the flap edge device, and how this device is mounted on the flap. The photograph of the Full Size Flap Tip Fence, which appears on the left of figure 4, shows the flap edge device from the side view. The line that appears on the flap edge device is drawn in only to illustrate the position of the surface of the Fowler flap when the flap edge device is mounted to the flap. The schematic on the right side of figure 4 illustrates the mounting of the Flap Tip Fence on the flap side edge.

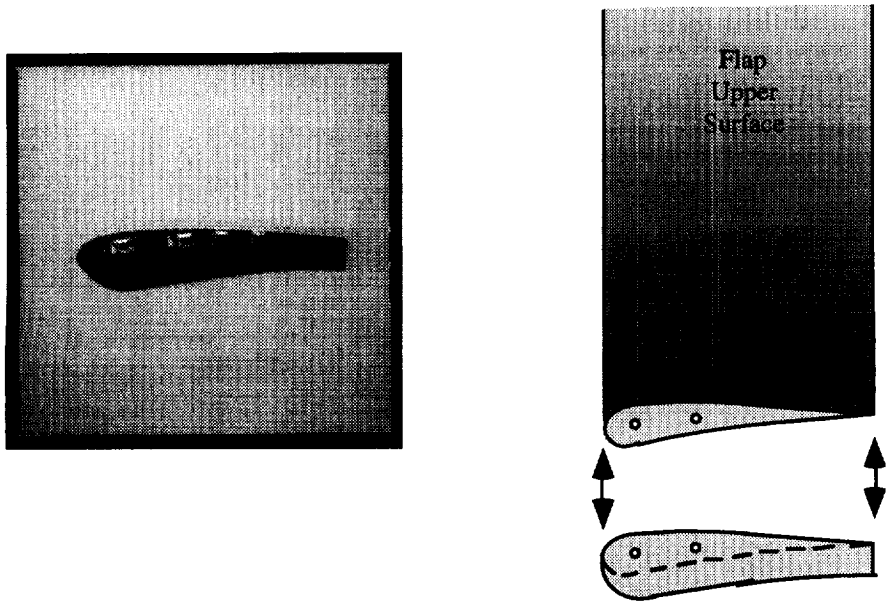

Figure 4. Photograph of Full Size Flap Tip Fence and illustration of mounting of Flap Tip Fence on flap model.

Both additions to the baseline configuration, the slat and the flap edge device were tested separately.

A variety of tests were performed by other groups around the baseline configuration. Among these tests were acoustic measurements, made with two different acoustic arrays of microphones. These acoustic measurements were done simultaneously with pressure tap surveys performed at fourteen cross sections along the span of the wing. Boundary layer flow visualization was accomplished with tufts placed on the surface of the model, as well as with surface shear stress visualization accomplished by using Liquid Crystal Coatings (LCC). Other tests included seven hole pressure probe wake surveys, hotwire surveys around and near the flap edge, and also Doppler Global Velocimetry (DGV). Particle Image Velocimetry closed out the set of measurement techniques.

The freestream flow characteristics were determined from settling chamber pressure taps, and a pressure tap ring between the ground planes upstream of the model. The configurations tested were the baseline configuration, (i.e., solely the wing and the half span flap), the baseline with the addition of the 3/4 span slat, and the baseline configuration with the flap edge device attached to the flap, as detailed in Table 1. The freestream flow conditions were characterized by the dynamic pressure head that was maintained at 40 psi. This corresponded to a freestream velocity of 64.84 m/s (w_∞).

Table 1. Summary of test conditions.

Configuration:	Characteristics	Freestream Conditions
Baseline (Wing & Flap)	Wing- 63_2-215 Mod B Span- 5 feet Chord- 2.5 feet 10° angle of attack Flap- Fowler Flap Span- 2.5 feet Chord- 0.75 feet 39° angle of attack	64.84 m/s
Baseline & 3/4 Span Slat	Slat- LB-546 Span- 3.75 feet Chord- 0.375 feet 10° angle of attack	64.84 m/s
Baseline & Flap Edge Device	Full Size Flap Tip Fence	64.84 m/s

The PIV setup used for testing is illustrated in figure 5, while figure 2 illustrates the PIV set up relative to the wind tunnel. The PIV setup was mounted on the floor of the tunnel, so that the apparatus extended up from the floor. This was done to stabilize the set up from vibrations of the test section. The position of the optics rail along the x direction on the tunnel floor was determined based upon analysis of vortex data taken from a prior experiment. From the previous experiment, Flap Edge I, we were able to determine the approximate position of the center of the vortex, and this information was used to position the optics rail in the x direction, and also to position the collection optics pod at the appropriate height. (Flap Edge I primarily studied only the baseline configuration.) The flow field illuminated by the laser sheet was imaged by the CCD camera at a distance of approximately 1.62 meters.

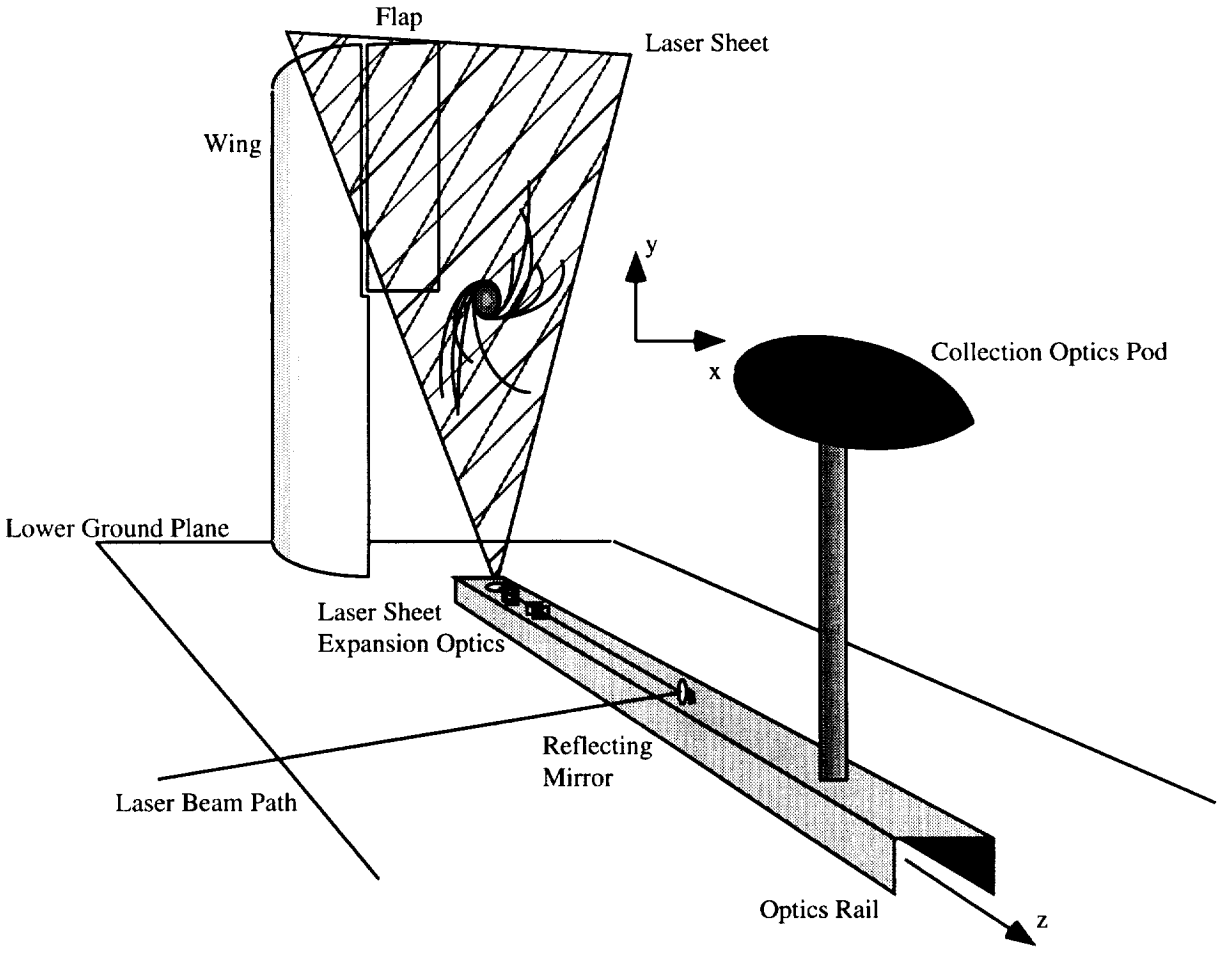

Figure 5. Experimental Setup

The laser light source was placed exterior to the wind tunnel test section. The laser used in this setup was a Spectra Physics PIV - 400 Nd:Yag double pulsed laser, which had an output at maximum power of approximately 870 mJ per pulse. The laser was frequency doubled to produce 532 nm wavelength light from a beam that was originally composed of 1032 nm wavelength light. The laser light passed through the tunnel wall as a coherent beam, and then expanded into a laser sheet by a suitable optics package. The optics package used to create the laser sheet was attached to the optics rail that was mounted on the floor of the test section. (The rail was designed to permit several downstream flow cross sections to be studied, but test time constraints did not allow this to be carried out.) The optics package used to create the laser sheet consisted of four cylindrical lenses. Two cylindrical lenses were used to control the thickness of the laser sheet, which was approximately 0.5 mm thick. The second set of two cylindrical lenses was used to spread the laser beam into a sheet. The optics used to expand the laser beam to a sheet were protected from the freestream flow by a cowling assembly. The laser sheet was oriented perpendicular to the primary flow. This orientation yielded data for the cross flow velocities. Using the wind tunnel coordinate axis illustrated in figure 5, and the corresponding u, v, and w velocity components, the cross plane velocity data calculated corresponds to the u and v components. For this test the laser sheet was 18 inches downstream of the flap trailing edge.

The tracer particles used for this experiment were generated by two Roscoe 4500 fog machines. These smoke generators are typically used for theatrical presentations. The particle sizes obtained from these smoke generators are typically between 0.1 and 5.0 micrometers. The flow was seeded by placing the smoke generators in the settling chamber and the smoke was then entrained into the flow. Generally, it was only necessary to use a single smoke generator, but depending on the tunnel conditions, and in particular the tunnel temperature, sometimes it was necessary to use both smoke generators to seed particles within the core of the vortex.

Once the smoke was entrained into the vortex generated by the half span flap, the flow field was imaged by a high resolution CCD Camera. The camera used in this experiment was a Kodak Megaplus Camera, Model 4.2. This camera featured a 2029 (H) by 2044 (V) pixel array. The size of the individual pixel elements was 9 μm. For this experiment an image area of 2000 by 2000 pixels was used and this yielded a real image area of 15.5 inches square, or just under 40 cm. For each individual image the camera downloaded approximately 4 Mb images to an IBM Risc 6000 Work Station. This camera was used in conjunction with a specially designed lens, and was a four element objective in

Tessar lens form. The lens focal length was 75 mm with a F# of approximately 4. This yielded a focal depth of about 15 mm. The magnification was 24.45 x at a working distance of 1.9 m for recording of a 0.5 by 0.5 meter region. The collection optics set up is illustrated in figure 6.

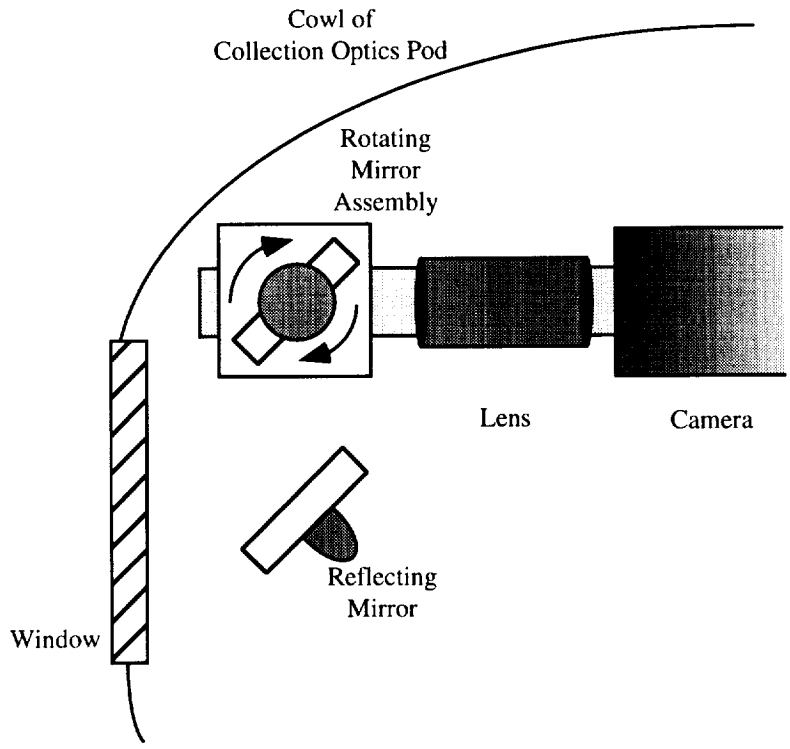

Figure 6. Collection Optics Set Up with the Collection Optics Pod.

This set up was housed in a protective aerodynamic cowl that protected the internal optics from the pressure forces of the freestream flow, and prevented smoke from coating the optical surfaces. The alignment of the optical axis and the focusing of camera was performed before closing the protective cowl.

As mentioned above an IBM Risc 6000 was used to store the images. The rotating mirror originated the timing sequence for capturing each image. The rotating mirror was operated at 10 Hz. When the mirror was at the proper position the rotating mirror would send a pulse to both the camera and the laser. The camera hardware upon receiving the

pulse would open the shutter of the camera. Likewise the laser power supply, upon receiving the signal from the rotating mirror hardware, would fire the first laser pulse. The second laser pulse was triggered by a unit, which introduced a time delay, Δt between pulses, as set by the user. The shutter of the camera was then closed after the second laser pulse leading to a double exposed image. This single image, with the artificial shift from the rotating mirror, was then downloaded to the computer. The computer had sufficient memory to allow a series of up to 30 images to be collected before it was necessary to save them to disk.

4. RESULTS

Figure 7 is presented to illustrate the type of raw data that was processed by the PIV software.

Figure 7. Double exposed single raw data image.

In figure 7 we note that the entire flow field is not saturated. Despite the apparent lack of particle uniformity throughout the flow field imaged, there are particles, and therefore data, in generally all regions of the image. In particular the core of the vortex contains particles which were imaged by the CCD camera. In most previous PIV studies of vortex flows, significant difficulty was encountered imaging the particles within the core of the vortex, and these difficulties in imaging the particles within the vortex core resulted in data drop out in the center of the vortex. The laser light intensity used in this experiment, which represented an order of magnitude increase in intensity over previous PIV lasers, overcame the difficulty of imaging the particles in the core of the vortex. The reason the laser light intensity solves the problem of imaging the vortex core is that generally the vortical flow structure will force larger particles to be thrown out of the core of the vortex. As a result only the smaller tracer particles remain in the vortex core. The primary difficulty in imaging these smaller particles has been getting sufficient scattered light from the particles onto the collection optics imaging plane. The laser used in this experiment, the Spectra Physics PIV - 400 Nd:Yag double pulsed laser, which actually contains two separate lasing elements, provided 870 mJ per pulse, and this proved to be sufficient light for imaging of the smaller particles in the vortex core. Figure 8 contains the velocity field calculated from the image in figure 7.

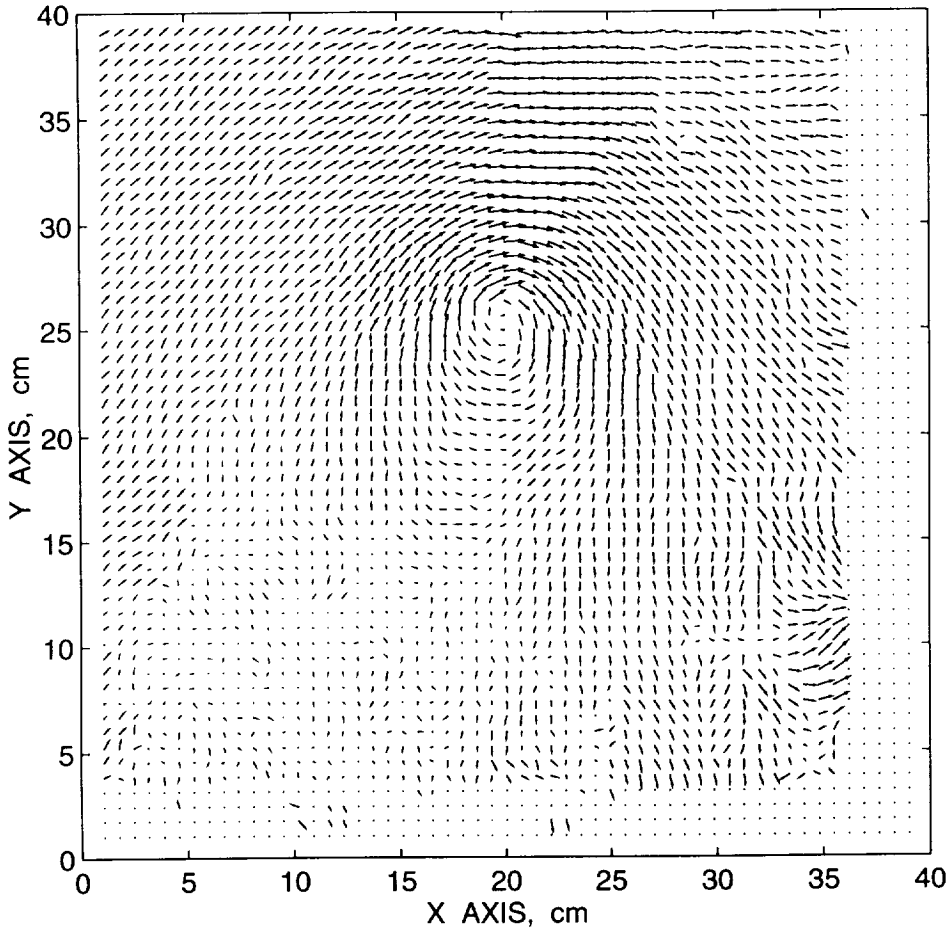

Figure 8. Velocity field calculated from figure 7 above.

The data drop out found along the perimeter of the velocity map is due to the triangular shape of the laser sheet. (See figure 5.)

Initially imaging the flow field illuminated by the laser sheet proved difficult, since the flow field to be measured was the cross plane flow, u and v components of velocity, and not in the primary freestream direction, w. It must be realized that in order to capture a good double exposed single image, a majority of the particles imaged by the first laser pulse must also be present when the second laser pulse is fired. If this is not the case the correlation function calculated, and used to determine the velocity, will yield a low maximum probability, and this will in turn increase the chance that an erroneous result is

determined. In this experiment the freestream flow serves to make imaging a large number of particles in both laser sheets difficult. In fact while performing the experiment it was discovered that the downstream velocity was accelerating significantly as the airflow interacted with the model. (Recall the freestream velocity upstream of the model was determined to be 64.84 m/s.) The downstream velocity component, w referenced in the coordinate system indicated in figure 5, was measured as approximately 100 m/s in the core of the vortex by the Doppler Global Velocimetry technique (DGV). This high speed flow presented difficulties for capturing particle pairs within the region of the two laser sheets when the two laser sheets coincided in the same plane. To overcome this problem it was determined that it would be beneficial to move the position of the second laser sheet downstream in order to capture the positions of the particles at the second instant in time. See figure 9, which shows a schematic of the method used to ensure the capture of the second position of the particles.

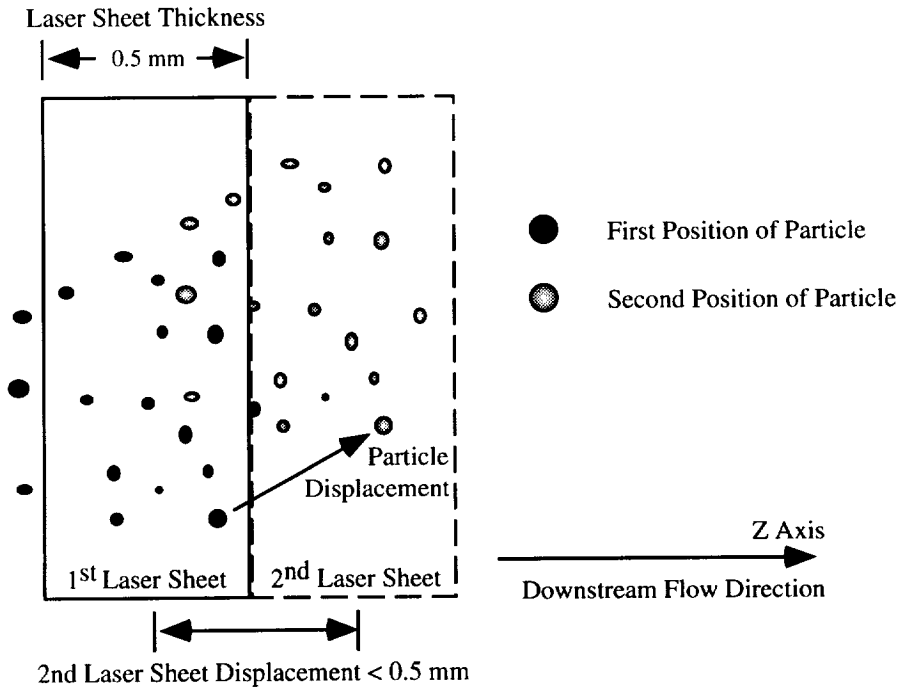

Figure 9. Schematic of second laser sheet displacement.

This solution of displacing the second laser sheet worked well, and was simple to institute. To displace the second laser sheet it was necessary to merely change the optical path of the second laser beam before the beam was frequency doubled to 532 nm. By changing the optical path before the frequency doubler we were able to create a small offset which was propagated across all the optics used to create the laser sheet, and therefore by using relatively small changes before the frequency doubler the second laser sheet was maintained parallel to the first sheet and still displaced as desired. Since this solution was devised during the experiment, and was not anticipated prior to the experiment, a precise measurement of the offset was not made, but rough measurements of the displacement determined that it was less than the width of a laser sheet which was measured as 0.5 mm.

In determining the velocity fields it was necessary to correct for the effects of the rotating mirror. The rotating mirror introduces perspective errors to the calculated velocity fields, and also creates additional magnification errors. These errors are systematic and can be predicted and corrected for in the calculation of the velocity field. Mehmet B. Alkislar, a graduate student at Florida State University was primarily responsible for determining the expressions used to correct the velocity data.

In order to express the corrections used it is necessary to first discuss the expressions used to determine the certain experimental variables and constants. The shift produced by the rotating mirror assembly can be calculated by first looking at the fundamentals of the experimental setup. This expression has been given previously, but it is repeated here for convenience.

$$X_{shift} = 2\,\omega\,R\,M\,\Delta t$$

The above expression can be used to calculate the horizontal shift of the particle positions captured by the second laser pulse. It is important to keep in mind that the velocity calculated by the correlation function is initially determined in terms of a displacement, and that dividing the displacement by the time interval between laser pulses determines the value of the velocity. As a result the initial quantity for the calculated 'velocity' is in fact a physical value of displacement. With this fact in mind the expressions for velocity are as follows.

$$u_{corr} = u_{calc} - X_{shift} - \varepsilon_x$$

$$v_{corr} = v_{calc} - \varepsilon_y$$

X_{shift} is the spatial shift introduced by the rotating mirror. The epsilon factors are the error terms introduced by the rotating mirror. The subscript 'calc' terms designate the calculated velocity from the application of the correlation function. The subscript 'corr' designates the corrected velocity values. The expressions for the error corrections, the epsilon factors, are as follows.

$$\varepsilon_x = (x + X_{shift})\,(x + CM)\,B_s$$

$$\varepsilon_y = y\,(x + CM)\,B_s$$

$$B_s = \frac{2\,\omega\,\Delta t}{F\,(1 + M)}$$

These corrections are applied pointwise. x and y are the coordinates of the point of interest in the image. The axes are defined centered on the image with the point (0,0) in the center of the image. C is the misalignment between the axis of the mirror and the optical axis, and was zero in this experiment. Note that some terms referenced here are illustrated in figure 1. M is the magnification, which is defined as

$$M = \frac{A}{B},$$

where A and B are the distances between the lens and the recording plane and between the lens and the image plane respectively. Δt is the time between the two laser pulses. R is the distance between the mirror axis and the measurement plane. F is the focal length of the lens, and from the Gaussian form of the thin lens equation is defined as

$$\frac{1}{F} = \frac{1}{A} + \frac{1}{B}.$$

ω is the angular speed of rotation of the mirror. This rotating mirror correction is applied to all of the calculated velocities. Table 2 contains the constants used in the calculations for the errors due to the rotating mirror. Note that the distance between the mirror rotation axis and the measurement plane was not measured. This value, designate the variable name R, was not necessary for this error analysis or any other calculations. Recall that the value for the artificial shift, X_{shift}, is the only variable that explicitly relies on the value for R in order to calculate its value, and the artificial shift was calibrated during the test. X_{shift} is dependent upon the time delay, Δt, between laser pulses given that all other variables are constants in the expression for the artificial shift, and rather than depend on measurements

to calculate the value for the artificial shift it is simpler to merely calibrate for the value of X_{shift}.

Table 2. Summary of optical constants of the PIV system used in this experiment.

A (m) Distance from lens to image plane	B (m) Distance from lens to object plane	F (mm) Focal length of the lens	M Magnification	ω Angular Rotation Rate
0.078	1.716	75	0.0457	62.8

The epsilon error terms were calculated and the velocity values were corrected using the above formulas. It was found that the maximum errors were approximately one tenth of a pixel. (These pixel displacements are the basic displacement unit before scaling the displacements to real quantitative values of meters.) This value for the maximum error is compared to the minimum displacement measured throughout the experiment which was 5 pixels. Using these two extreme values it was determined that the extreme case would be that the perspective and magnification errors could accounted for a maximum error of approximately 2 %.

Figures 10, 11, and 12 present data for each of the three configurations tested. The first configuration is the baseline configuration. The baseline contains the wing at an angle of attack of 10°, and the flap at an angle of 39°. The second configuration is the baseline with the addition of the 3/4 span leading edge slat at an angle of attack of 10°. The third is the baseline with the addition of the flap edge device, (see figure 4 for reference).

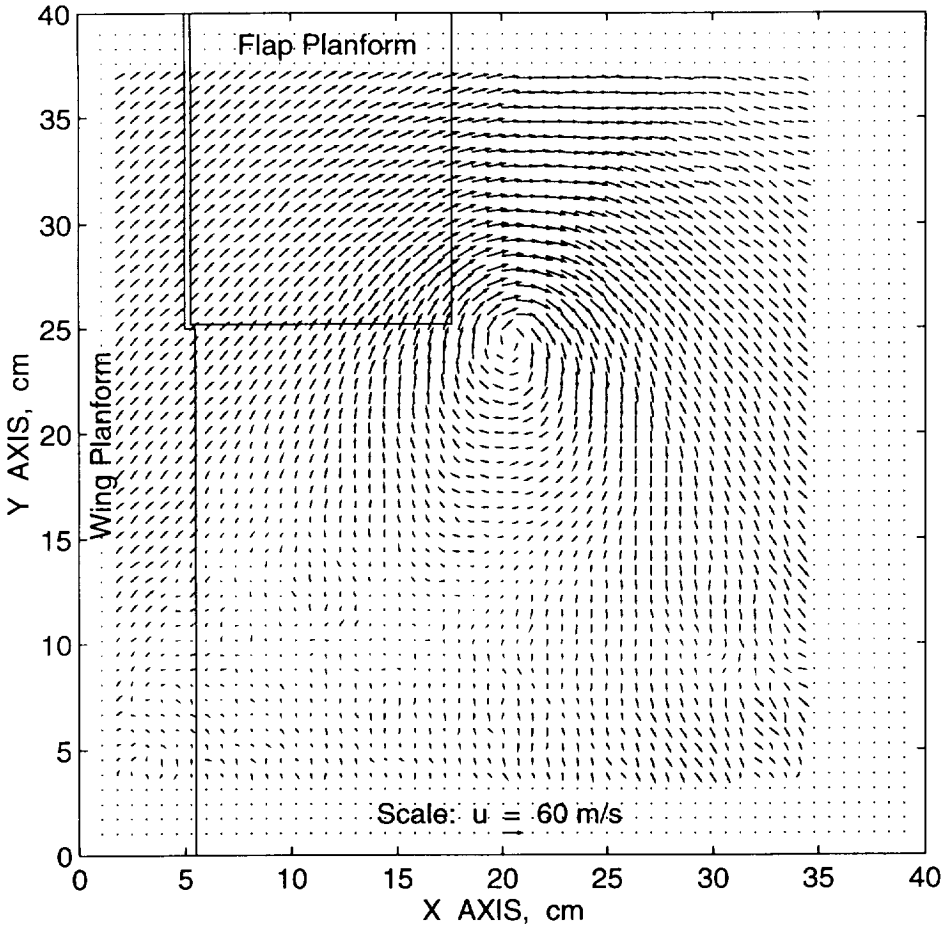

Figure 10. Baseline configuration velocity field at 18 inches aft of flap trailing edge.

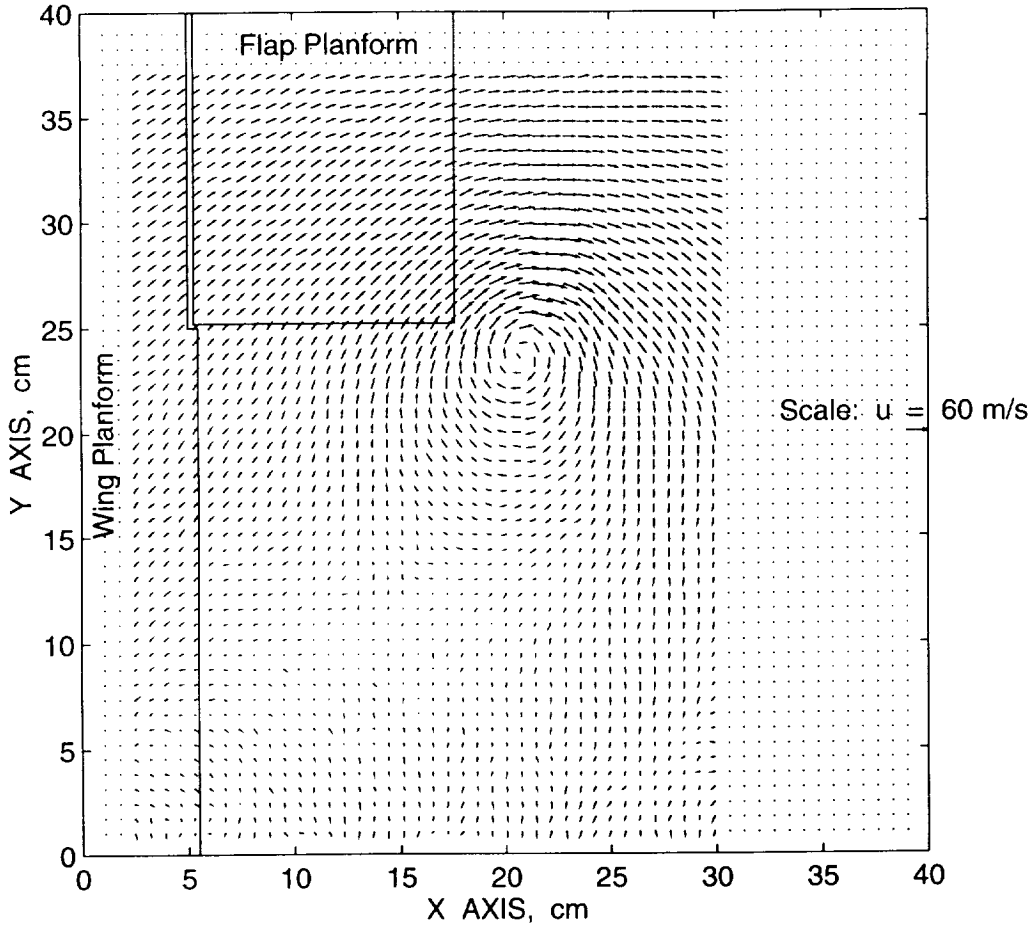

Figure 11. Baseline configuration with 3/4 span slat; Velocity field at 18 inches aft of flap trailing edge

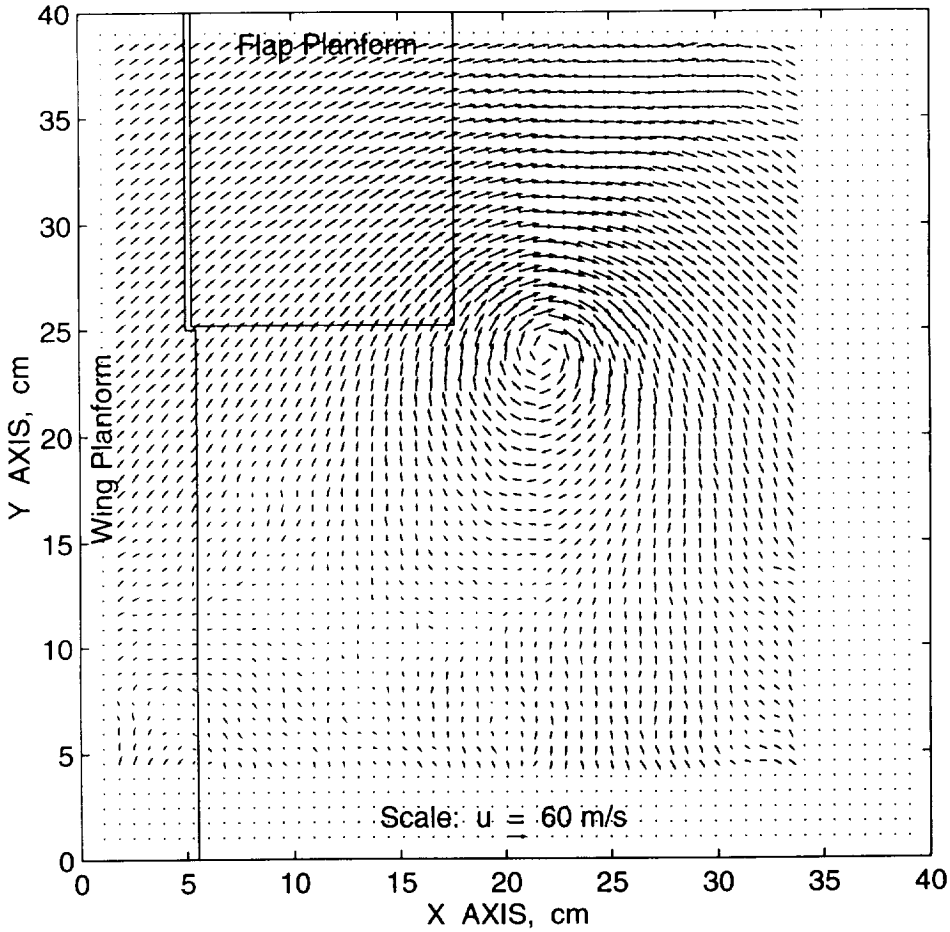

Figure 12. Baseline configuration with Flap Edge Device; Velocity field at 18 inches aft of flap trailing edge.

Each of the above velocity fields is an average of five images. The averaging scheme used requires a little explanation. In order to average the velocity fields it was first necessary to find the average center of the vortex. The center of the vortex for all schemes is defined as the point of minimum vorticity. (Note that for a vortex rotating in the clockwise direction in the coordinate system defined here, that the vorticity will have a negative value. This is the minimum vorticity referred to in the above discussion.) The average center of the vortex refers specifically to the average position of the minimum vorticity when considering all five velocity fields. The velocity fields for each of the five images did not necessarily predict the same point as the center of the vortex. Therefore it was first necessary to determine the average position where the vortex would be centered. Once this point was defined the images were shifted such that the center of the vortex for each of the five images was in the same position as the average center of the vortex, and then the five

images were averaged to produce figures 10-12. This scheme is perhaps a bit involved, but it maintains two pieces of information of interest. The average position of the vortex is still determined, and the calculated average vorticity still contains a relative measure of the vorticity distribution at one instant, whereas if the averaging were performed without centering each vortex some information would be lost.

In order to illustrate the quantitative content of the velocity fields of figures 10-12, figures 13-15 present horizontal and vertical slices through the center of each vortex for the three configurations tested. Note that the calculated center of the vortex is indicated in the figures.

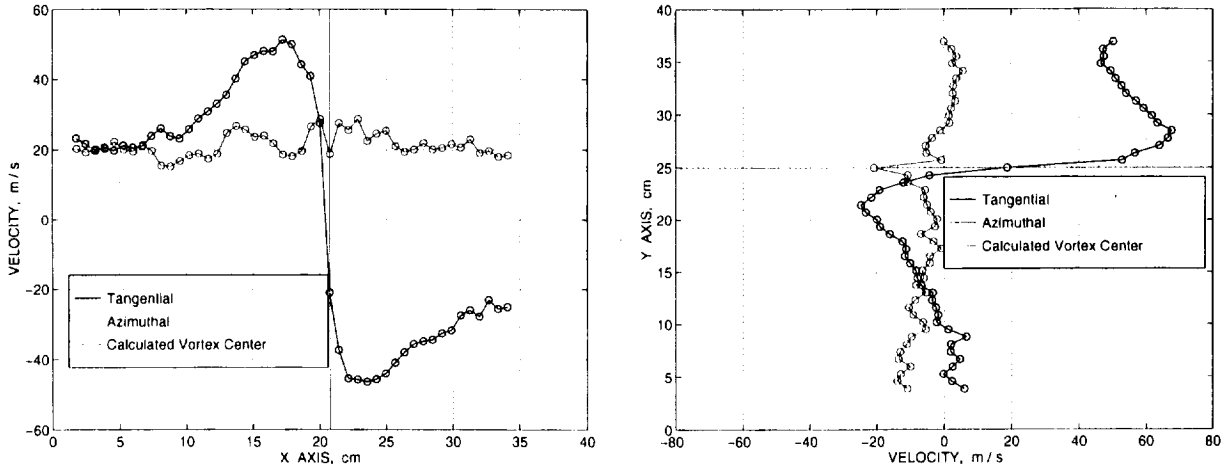

Figure 13. Baseline configuration; Velocity profiles at 18 inches aft of flap trailing edge.

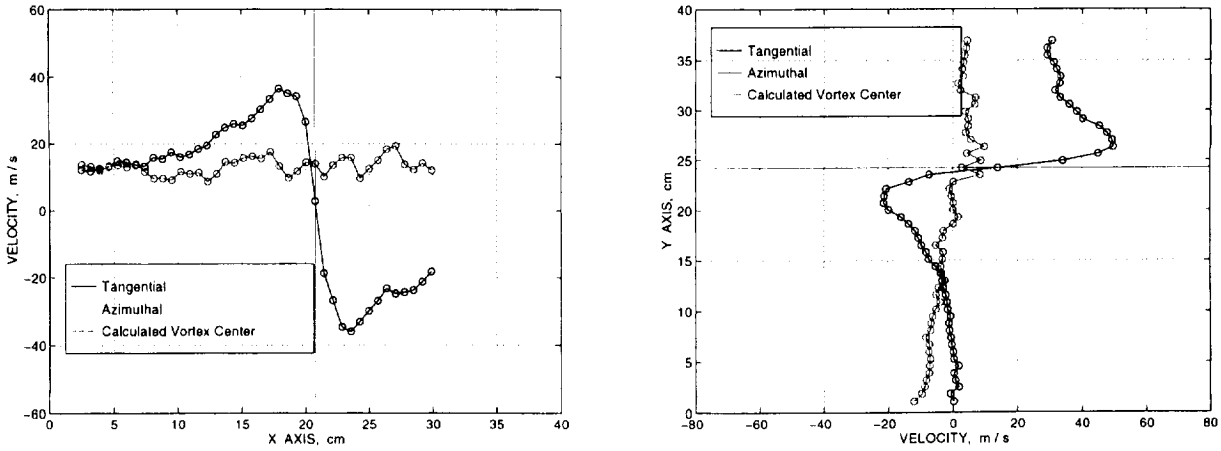

Figure 14. Baseline configuration with 3/4 span slat; Velocity profiles at 18 inches aft of flap trailing edge

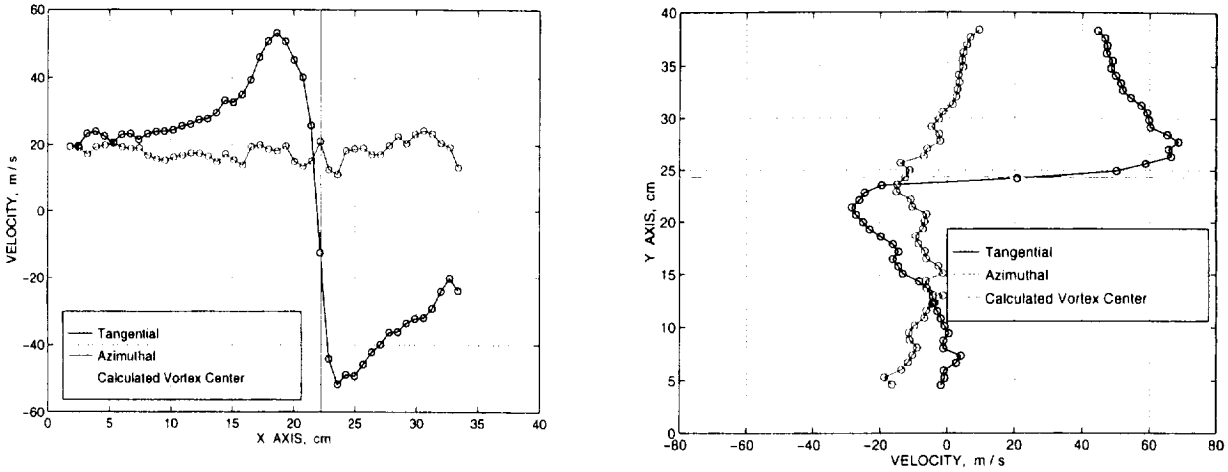

Figure 15. Baseline configuration with Flap Edge Device; Velocity profiles at 18 inches aft of flap trailing edge.

5. DISCUSSION

From the analysis used for determining the center of a vortex, it is immediately apparent that there is vortex wander. Numerous wind tunnel studies of vortices shed from half span wings also show vortex wander. Although no studies specific to a half span flap were found which addressed vortex wander, one can assume that similar factors would influence the wander of the vortex position shed from either source. One factor that contributes to vortex wander for half span wings was hypothesized to be wind tunnel turbulence levels. This seems to be a reasonable conclusion, but this influence has not be quantitatively evaluated, and factors other than turbulence must also play a role in determining the position of the vortex from one moment to the next. For the experiment carried out here, the relative motion of the vortex was measured to be on the order of 0.73 cm between frames, with the entire range of motion confined to a calculated area of approximately 0.42 cm^2. The wind tunnel turbulence levels were tested, and were determined to be 0.1%.

Other information found from the plots of the velocity field is the position of the center of the vortex relative to the flap trailing edge. Although this information can be determined from figures 10-12, it is simpler to determine the position of the vortex from a plot of vorticity. Figures 15-18 show the calculated average vorticity plots. (Note that in

each figure there is a mesh plot showing the levels of the vorticity, and an underlying contour plot which is primarily used to find the position of the center of the vortex downstream of the flap trailing edge.)

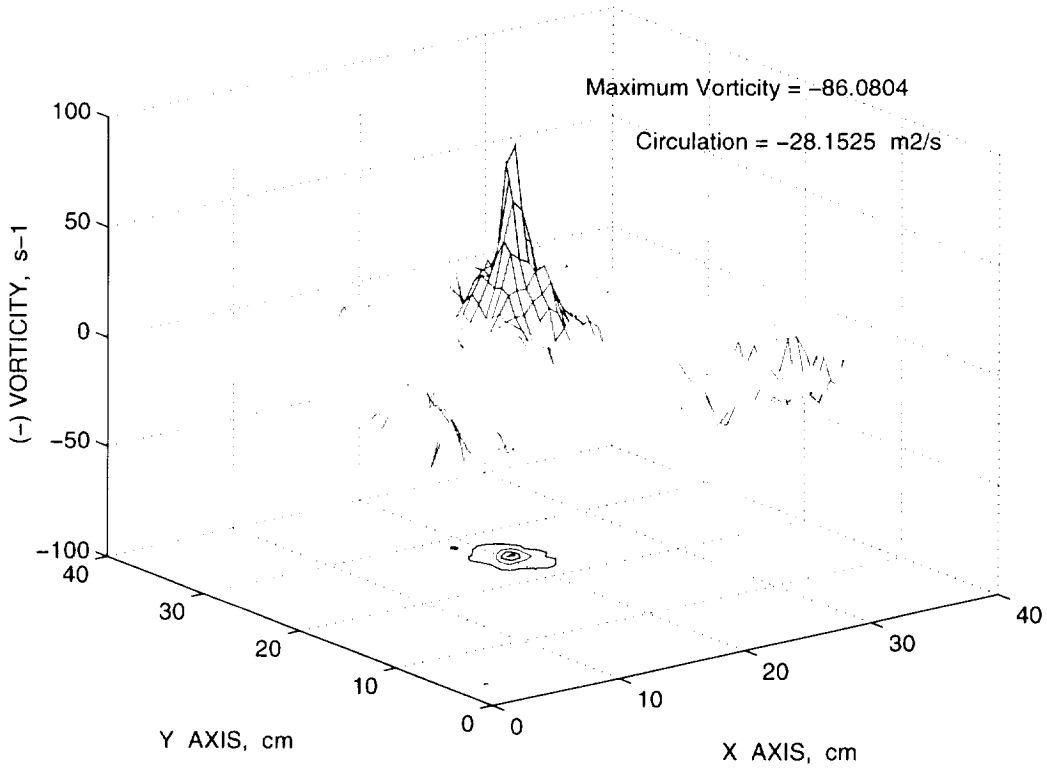

Figure 16. Baseline configuration. Vorticity distribution.

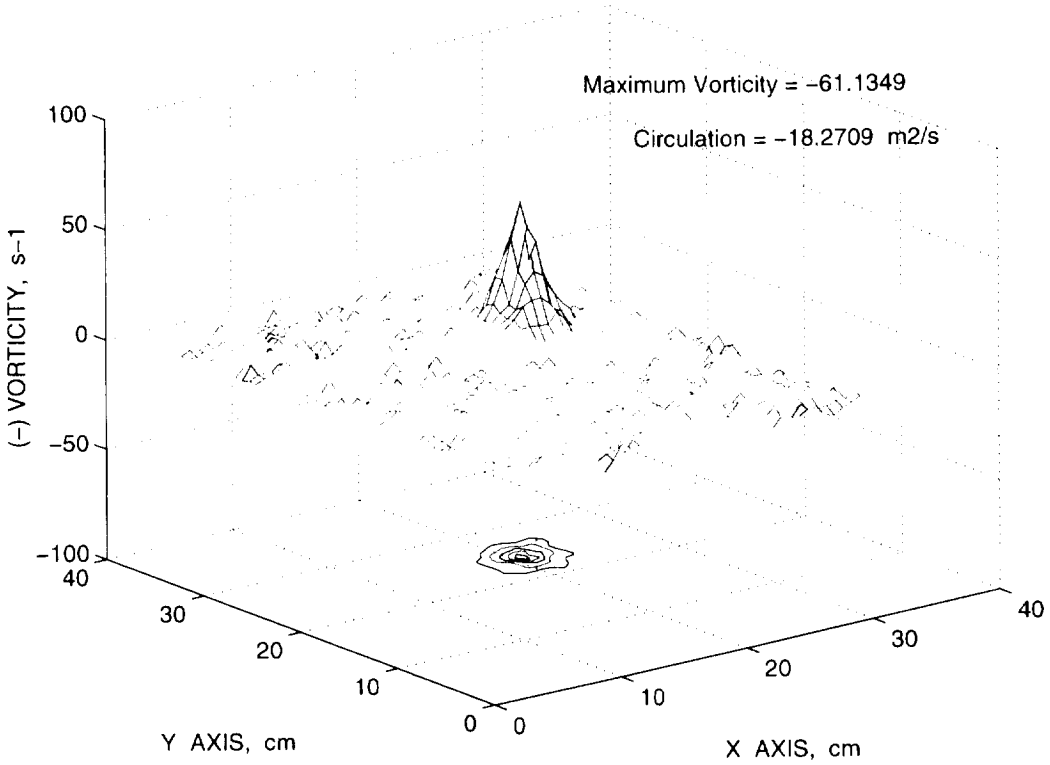

Figure 17. Baseline configuration with 3/4 span slat. Vorticity distribution.

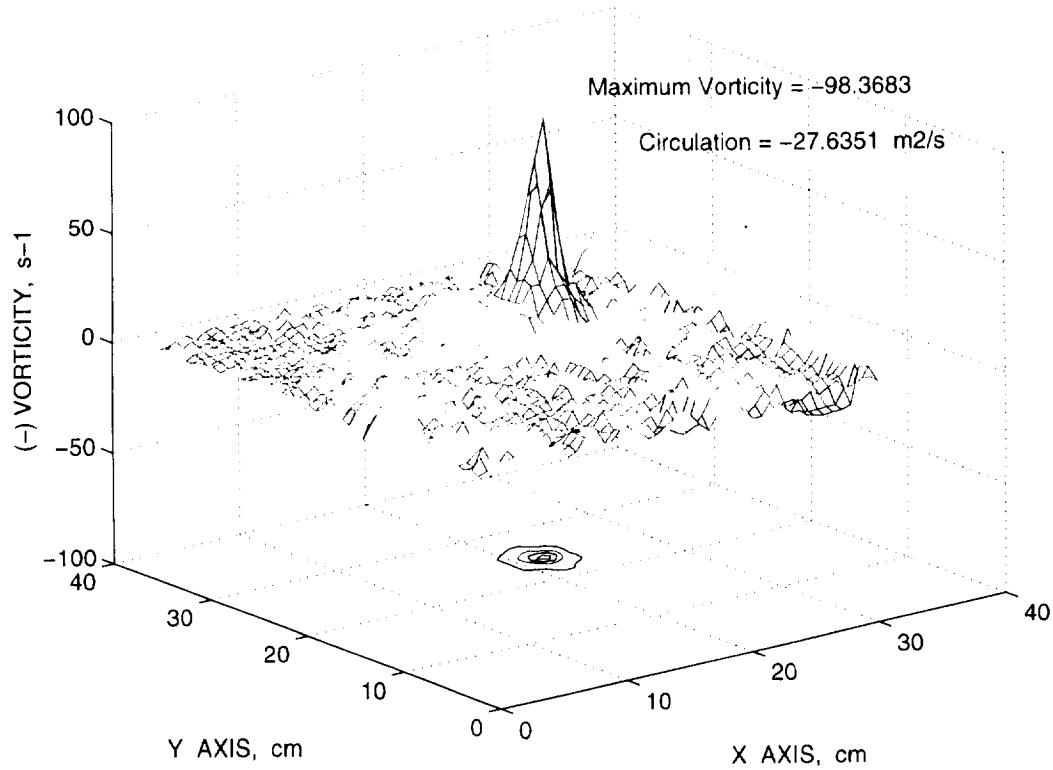

Figure 18. Baseline configuration with Flap Edge Device. Vorticity distribution.

From figures 16-18 the relative position of the center of the vortex downstream of the flap trailing edge is determined. (Recall that these measurements are taken at a position 18 inches downstream of the flap trailing edge.) The relative positions of the center of the vortex are reported in Table 3. These positions are given relative to the axes of figures 10-12.

Table 3. Relative position of the calculated center of the vortex.

	X Position (cm)	Y Position (cm)
Baseline Configuration	20.75	24.94
Baseline Configuration with 3/4 Span Slat	20.75	24.23
Baseline Configuration with Flap Edge Device	22.14	24.23

It is apparent that the motion of the center of the vortex at this position downstream is small. This data does not permit conclusions to be drawn, but the differences in positions will be pointed out and commented upon. These comparisons are referenced to the baseline configuration. For the case of the 3/4 span slat it is seen that the center of the vortex has not shifted in the x direction, but has moved vertically down in the y direction. This is most likely attributed to the interaction of the flap tip vortex with the vortex shed from the 3/4 span slat. The vortex shed from the 3/4 span slat will create a low pressure area most likely in the region below the flap, and this low pressure area may affect the flap tip vortex by causing its motion to proceed in the negative y direction. The case of the Flap Edge Device shows that the vortex has moved in the positive x direction and in the negative y direction, when referenced to the baseline configuration. It is apparent that the Flap Edge Device will affect the roll up of the flap tip vortex, and any change in the position of the vortex for the configuration with the Flap Edge Device is likely attributed to this change in roll up. These conclusions are of course only hypotheses, but the results presented here do suggest that further studies are necessary in order to precisely determine the position of the center of the vortex for the configurations tested.

It was hoped that the velocity field of figure 11 would also yield information related to the vortex that was shed from the edge of the 3/4 span slat. This was not the case. There was no apparent second vortex in the velocity field of figure 11, nor was there any evidence of another source of vorticity in figure 17. This could be due to one of two factors. The first is merely that the vortex shed from the 3/4 span slat is not in the measurement plane. The second is that the vortex shed from the slat is diffused through interaction with the viscous boundary layer of the wing. In any event it is not known what occurs with the slat vortex. Further studies are needed to track the position of the slat vortex and the interaction of the slat vortex with the downstream flow field.

We also attempted to determined the circulation from the vorticity data. The circulation calculated is a rough approximate. Although it is expected to be a rough estimate, the calculated values for circulation are rough primarily due to the limited number of images averaged. With merely five images the average vorticity fields calculated still have significant noise levels, and this noise corrupts the circulation determined from the vorticity data. Looking at figures 16-18 it can be seen that the vorticity outside the core of the vortex does not fall monotonically towards zero as expected. Instead the plots of figures 16-18 show vorticity levels that approach zero, and oscillate near and around zero. Figures 19-21 show vertical cross sections of the vorticity data found in figures 16-18. These figures are included only to point out the presence of noise as mentioned above.

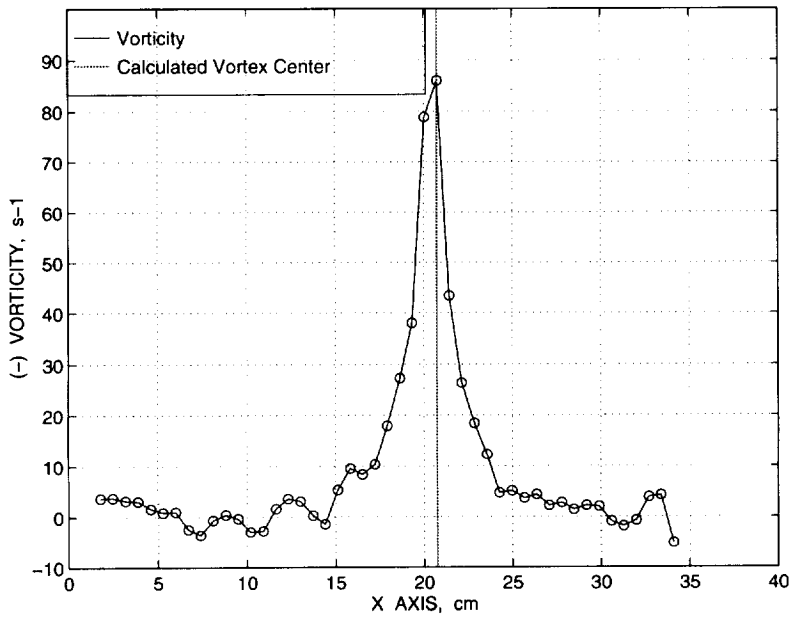

Figure 19. Baseline configuration. Horizontal vorticity profile through the center of the vortex.

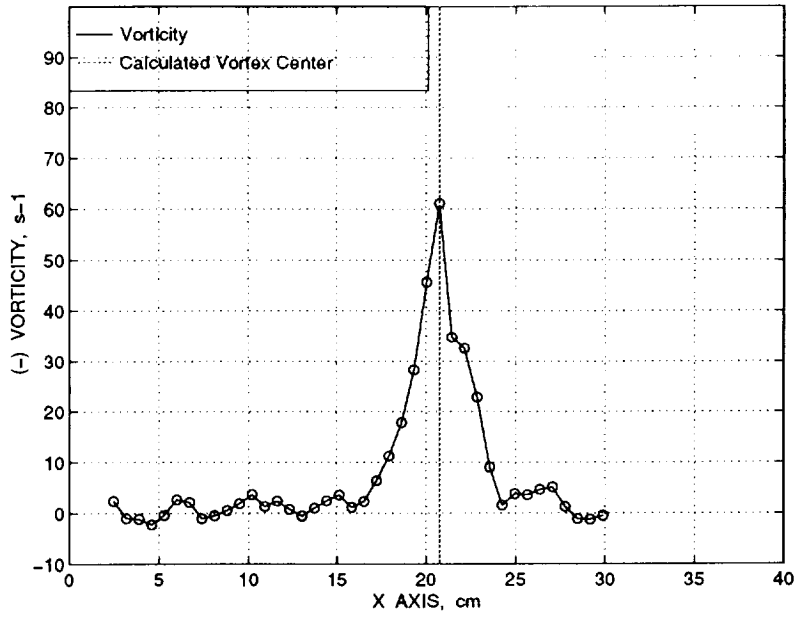

Figure 20. Baseline configuration with 3/4 Span Slat. Horizontal vorticity profile through the center of the vortex.

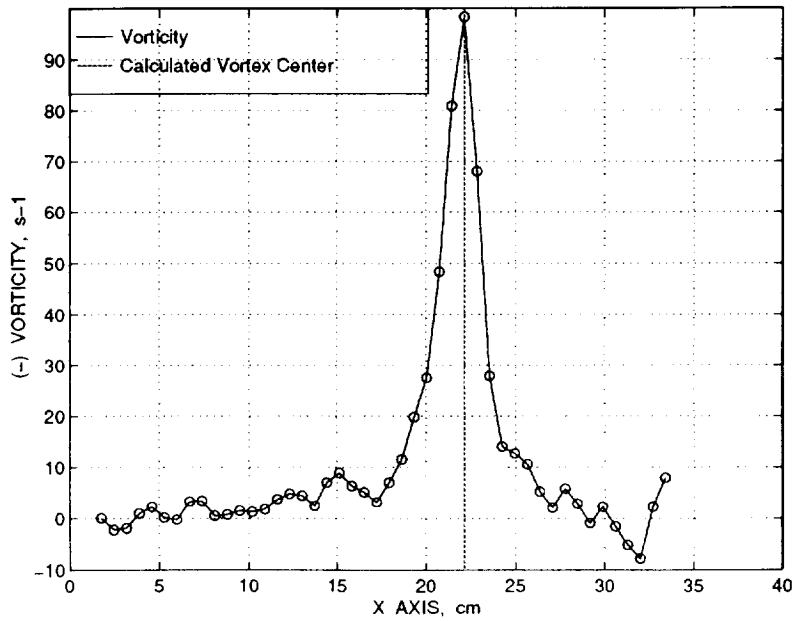

Figure 21. Baseline configuration with Flap Edge Device. Horizontal vorticity profile through the center of the vortex.

In order to limit the effects of noise on the calculated circulation, the circulation was only calculated over a finite area of the entire vorticity field. The scheme used to determine the integration area simply limited the area of integration to the region in which the vorticity values were greater than the noise levels measured around the periphery of the entire velocity field. This method was used to calculate the circulation and these values are listed in Table 4.

Table 4. Circulation values for each configuration.

	Circulation (m^2/s)
Baseline Configuration	-28.15
Baseline Configuration with 3/4 Span Slat	-18.27
Baseline Configuration with Flap Edge Device	-27.63

For the case of the 3/4 span slat the circulation from the flap has been significantly reduced from the baseline configuration. This is most likely due to changes of the flow field around the wing, which in turn affects the flap tip flow characteristics. The overall circulation of the baseline configuration with the 3/4 span slat has most likely increased, but the flap itself is responsible for less of a contribution to the overall circulation than for the baseline configuration. The most important conclusion drawn concerning the flap edge device is that it did not cause an appreciable reduction or increase of the circulation. A marked change in the circulation would indicate a change in the lift characteristics associated with the configuration change. This result is significant, but when taking into account that the flap edge device resulted in a 3 dB decrease in the noise generated by the flap edge, then it appears that the flap edge device proves to be a viable scheme for noise reduction, and one which does not effect the lifting characteristics of the flap itself.

6. CONCLUSIONS

The PIV method and setup developed for the 7 by 10 foot wind tunnel has produced useful data concerning the flow field behind a multi-element airfoil. The airfoil coupled with the half span flap was tested in two other configurations, which were being tested primarily to identify noise sources, but provided an excellent opportunity for demonstrating the capabilities of the PIV method. From the data gathered during the experiment conducted using PIV, two primary concerns were examined, and these were 1), the positions of the center of the vortex behind the half span flap under different configurations, and 2) characterizing the circulation due to the flap tip vortex. Both results aided in answering two concerns of other researchers studying the multi-element airfoil. These results served to verify that practical data could be gathered from the PIV method. The experiment also served to show that PIV has matured to a level such that it can now be applied to large scale studies, 40 x 40 cm, and furthermore, measurements can be made in the cross plane flow direction.